frontiers | Frontiers in Energy Research

ORIGINAL RESEARCH
published: 03 June 2022
doi: 10.3389/fenrg.2022.883882

Understanding the Formation Process of Perovskite Layers Grown by Chemical Vapour Deposition

*T. Moser[1], R. Kothandaraman[1], S. Yang[1], A. Walter[2], S. Siegrist[1], H. Lai[1], E. Gilshtein[1], A. N. Tiwari[1] and F. Fu[1]**

[1]*Laboratory for Thin Films and Photovoltaics, Empa—Swiss Federal Laboratories for Materials Science and Technology, Dübendorf, Switzerland,* [2]*CSEM—Swiss Center for Electronics and Microtechnology, Neuchâtel, Switzerland*

This work aims at extending the understanding of the formation processes of $(Cs_{0.07}FA_{0.93})PbI_3$ perovskite layers deposited by a two-step vapour method. In a first step, an inorganic CsI/PbI_2 precursor stack is deposited by thermal evaporation (TE). A chemical vapour deposition (CVD) is then used to convert the precursor into the perovskite layer by reaction with a chemical vapour of formamidinium iodide (FAI). Here we show how crystallinity and morphology of the TE precursor layer are both influenced not only by the substrate surface properties but also by the thermal treatment in the initial phase of the CVD process. Furthermore, we provide insights on the evolution of perovskite film formation and show how a uniform elemental composition is achieved by the diffusion of cesium through PbI_2 during the CVD conversion reaction.

Keywords: perovskite, thermal evaporation, chemical vapour deposition, film growth, PSC, vapour processing

OPEN ACCESS

Edited by:
Jovana V. Milic,
Université de Fribourg, Switzerland

Reviewed by:
Thomas Stergiopoulos,
Aristotle University of Thessaloniki, Greece
Tae Joo Shin,
Ulsan National Institute of Science and Technology, South Korea

****Correspondence:***
F. Fu
fan.fu@empa.ch

Specialty section:
This article was submitted to Solar Energy, a section of the journal Frontiers in Energy Research

Received: *25 February 2022*
Accepted: *10 May 2022*
Published: *03 June 2022*

Citation:
Moser T, Kothandaraman R, Yang S, Walter A, Siegrist S, Lai H, Gilshtein E, Tiwari AN and Fu F (2022) Understanding the Formation Process of Perovskite Layers Grown by Chemical Vapour Deposition. Front. Energy Res. 10:883882. doi: 10.3389/fenrg.2022.883882

1 INTRODUCTION

High hopes are put in the technology of hybrid organic-inorganic perovskite solar cells (PSCs). On the lab-scale, the record power conversion efficiency (PCE) of PSCs (25.7%) has caught up with the well-established crystalline silicon (c-Si) solar cells (26.7%) (Yoshikawa et al., 2017; National Renewable Energy Laboratory, 2020; Jeong et al., 2021). However, such lab-scale record PSCs are obtained on a small active area, typically lower than 0.1 cm (Jeong et al., 2021; Liu et al., 2021a; Zhang et al., 2021a; Guo et al., 2021; Yoo et al., 2021). Looking at record devices with larger active area, one sees that PSC are still lacking behind (Park and Zhu, 2020). Therefore, further research is needed to identify possible routes to fabricate PSCs with a very high quality over larger areas.

Various scalable approaches such as blade coating (Razza et al., 2015; Siegrist et al., 2021), slot-die coating (Du et al., 2020; Patidar et al., 2020), inkjet printing (Eggers et al., 2020; Schackmar et al., 2021), spray-coating (Heo et al., 2016; Bishop et al., 2020a; Bishop et al., 2020b), thermal evaporation (TE) (Chiang et al., 2020; Li et al., 2020; Feng et al., 2021) and chemical vapour deposition (CVD) (Liu et al., 2021b; Luo et al., 2021; Sahli et al., 2021) for the fabrication of PSCs have already been reported. The vapour-based deposition methods (i.e., TE and CVD) are very promising as they are scalable (i.e., already used on the industrial scale) (Powell, 2006; Ávila et al., 2017) and allow conformal coating on textured or rough surfaces. This is an essential requirement when aiming at integration of PSCs into monolithic tandem solar cell technology. There, c-Si and CIGS are possible bottom cells, which feature this type of surface morphology (Jošt et al., 2020; Kothandaraman et al., 2020).

However, the deposition of high quality perovskite absorber layers by co-evaporation of the inorganic and organic components requires high control of the individual evaporation sources, due

to the high volatility of the organic components, which poses a major challenge for the controllability and reproducibility of the process (Hoerantner et al., 2019; Swartwout et al., 2019; Liu et al., 2021b). To bypass this problem, one can separate the deposition steps of inorganic and organic constituents. In such a two-step process, an inorganic precursor (i.e., lead halides and/or cesium halides) layer is first deposited by thermal evaporation (i.e., at a pressure of a 10^{-7}–10^{-5} mbar, typically with the substrate at room temperature). A CVD process is then used to react the inorganic precursor with the vapour of an organic precursor (e.g., formamidinium iodide) to form the perovskite absorber. This process is usually carried out at medium vacuum (0.1–10 mbar) at which the flux of organic vapour is much more controlled than under high vacuum conditions. The substrate can be heated during the vapour transport/reaction step and the ambient can be controlled with inflow of gas/air for vapour transport.

The perovskite formation by chemical vapour was first reported by Chen et al., in 2013 as "vapour-assisted solution process" (VASP) (Chen et al., 2014). Shortly after, Leyden et al. reported 'hybrid chemical vapour deposition' (H-CVD) (Leyden et al., 2014), where they used a multi-zone tube furnace as reactor. The underlying concept behind other processes, such as *in-situ* tubular CVD (IT-CVD) (Luo et al., 2015) or low pressure hybrid CVD (LPHCVD) (Shen et al., 2016) remained generally same: A metal halide precursor is deposited by spin-coating or thermal evaporation and then converted to perovskite by reaction with a vapour of organo halides. In 2021, PSCs with efficiencies of 18.1% (Liu et al., 2021b; Wei et al., 2021) and even 19.59% (Luo et al., 2021) have been reported, showing the potential of CVD for PSCs.

As most of these reports usually focus on the power conversion efficiency of the final perovskite solar cell, only little investigations on the perovskite formation mechanism have been presented so far. Sahli et al. reported that a higher substrate temperature leads to larger perovskite grains (Guesnay et al., 2021). Liu et al. also observed a changed perovskite morphology depending on the employed organo halide precursor and hypothesized about the changes to the formation process due to different working pressures during CVD (Liu et al., 2021b). In our previous work, we have uncovered that a low substrate temperature in combination with long conversion times promote the formation of undesirable additional phases (Moser et al., 2020). In this paper we further elucidate the perovskite formation process: We first show that the structural properties of the metal halide precursor are determined by both the substrate surface properties it is evaporated on and the annealing during the heat-up of the CVD reactor, thus affecting the result of the CVD conversion process. We then present the top to bottom evolution of the reaction front during the CVD processs occuring in a planar fashion. We observe that during the conversion process the perovskite morphology is formed already in the initial stage and is maintained even beyond the point of full conversion. Concurrent to the conversion reaction, cesium diffusion through PbI_2, allows for the formation of compositionally uniform perovskite.

2 RESULTS AND DISCUSSION

2.1 Deposition of Metal Halide Precursor by Thermal Evaporation

In this section, we present our investigations on the metal halide precursor layer, which is formed by sequential thermal evaporation of 15 nm CsI and 300 nm of PbI_2.

2.1.1 Influence of the Annealing of NiO on the Structural Properties of Metal Iodide Precursor

The CsI/PbI_2 precursor is deposited on glass/ITO substrates coated with a 20 nm thick sputtered NiO layer. NiO is commonly employed as hole transport layer (HTL) in hybrid perovskite solar cells (Saranin et al., 2021; Mann et al., 2021; Boyd et al., 2020; Abzieher et al., 2020; Ma et al., 2021; Pang et al., 2019; Zhang et al., 2021b; Aydin et al., 2018). In undoped NiO the optoelectronic properties are determined by its defect chemistry (i.e., Ni and Oxygen vacancies) (Zhao et al., 2019). In the case of thin films, annealing treatments can be used to induce reaction of NiO with oxygen and humidity from the ambient, changing said defect chemistry (Zhao et al., 2019; Niu et al., 2018). In this work we use an annealing treatment to the NiO coated substrates for 15 min at 100, 200 or 300°C in ambient air. Hence, we refer to the different samples as **pristine NiO**, **NiO100**, **NiO200** and **NiO300**, to the NiO coated substrate being used in its pristine state (i.e., without annealing) or after the annealing at 100, 200 and 300°C, respectively. **Supplementary Figure S1A** shows the change of optical absorptance of upon annealing. For NiO100 there is no obvious effect, while for NiO200 and NiO300 the absorptance is clearly reduced with respect to the pristine NiO. This effect is attributed to a reduction of crystallographic defects (Newman and Chrenko, 1959). The annealing at or above 200°C is therefore a promising treatment to reduce the parasitic absorption by NiO in complete solar cells. In **Supplementary Figure S1B** we display scanning electron microscopy (SEM) top view images of the NiO layers. While the transparency of the NiO is improved by annealing, no structural changes (e.g., grain growth or cracking) are observed.

In 2015, Fu et al. reported that the choice of substrate has a strong effect on the morphology of evaporated PbI_2. It was found that a compact morphology with oriented platelets is developed on amorphous substrates, while a disordered state is formed on a crystalline substrate. To understand the effect of the NiO coated substrates on the structural properties of the sequentially evaporated CsI/PbI_2 layer, X-ray diffraction (XRD) and SEM were conducted. The investigation reveals that annealing of the NiO has a profound effect on the morphology and crystallinity of the CsI/PbI_2 precursor layer. The SEM top-view and cross-section images presented in **Figures 1A–D** show a change from a compact, layered morphology on the pristine NiO to a disordered, rough morphology on NiO300. This morphological trend is also accompanied by changes in crystallinity observed in the XRD measurements. **Figure 1E** displays the full width at half maximum (FWHM) and maximum intensity of the (001) peak of the PbI_2 phase. By the widening (i.e., increase of the

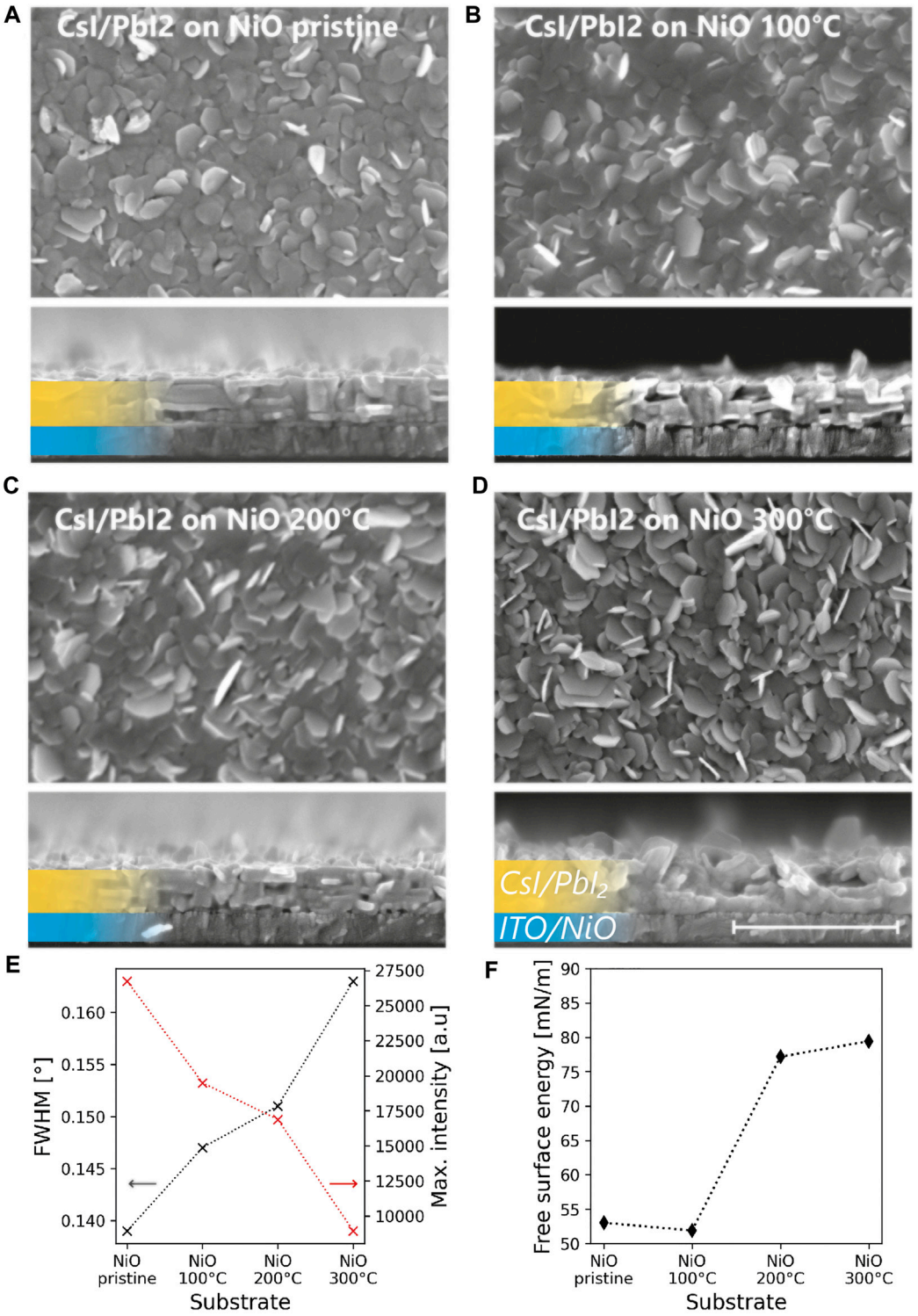

FIGURE 1 | Effect of annealing of NiO HTL on the CsI/PbI_2 precursor. SEM top view and cross section of CsI/PbI_2 precursor on **(A)** pristine NiO and NiO annealed at **(B)** 100°C, **(C)** 200°C and **(D)** 300°C. The morphology changes from layered and compact on pristine NiO to disordered and rough on NiO annealed at 300°C. The scale bar shows a length of 1 μm and applies to all SEM images. **(E)** Full-width-at-half-maximum and maximum intensity of the (001) diffraction peak of PbI_2 grown on pristine and annealed NiO **(F)** Surface free energy of the pristine and annealed NiO surfaces measured by contact angle measurements.

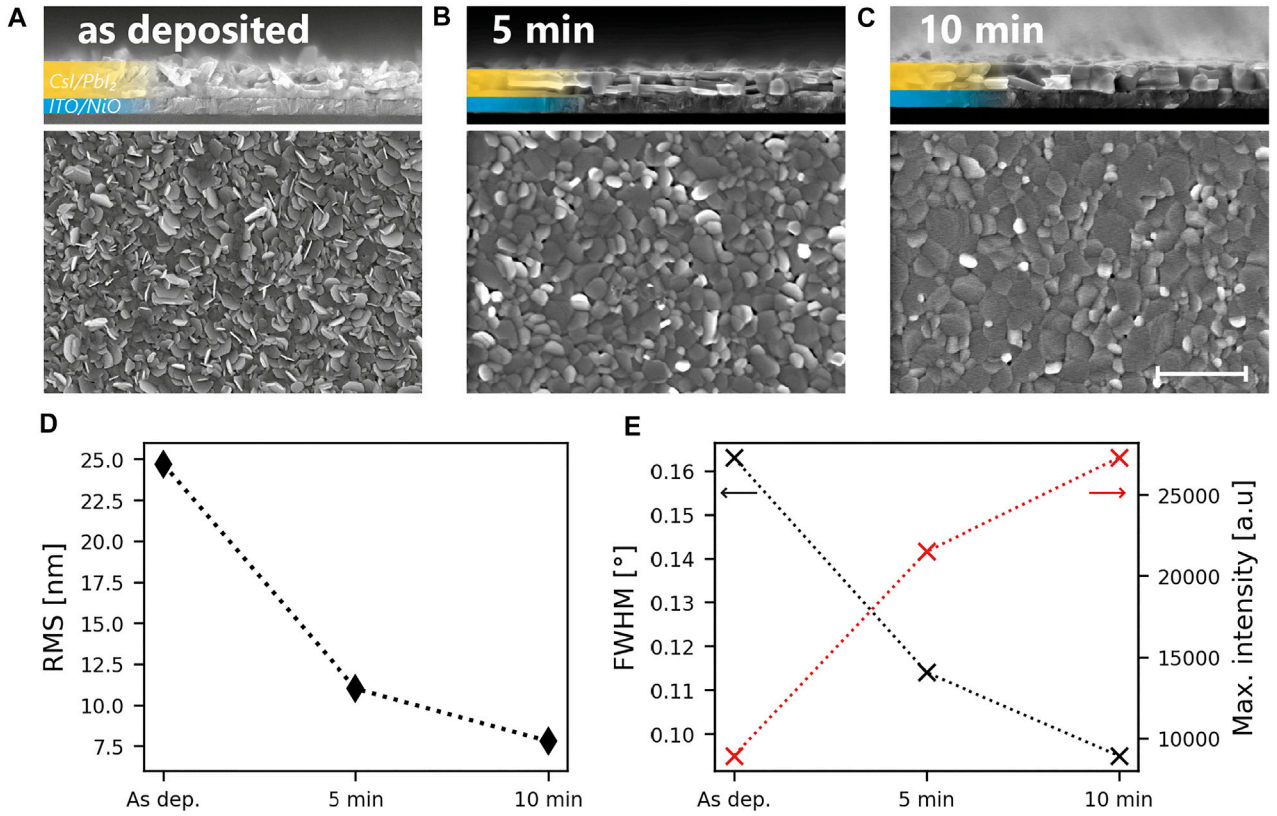

FIGURE 2 | Effect of annealing in the CVD system on the precursor. SEM cross section, top view as well as AFM scans of a CsI/PbI_2 precursor deposited on NiO annealed at 300°C in its **(A)** pristine state and after **(B)** 5 and **(C)** 10 min of annealing in the CVD system (170°C, 7 mbar). The scale bar shows a length of 1 µm and applies to all SEM images **(D)** RMS roughness extracted from AFM measurements conducted on the as deposited and the annealed precursor. **(E)** Full-width-at-half-maximum and maximum intensity of the (001) diffraction peak of PbI_2 of the layers in **(A–C)**.

FWHM) and a decrease in maximal intensity of the reflection peak, we see that the crystallinity of the precursor layer is highest on the pristine NiO and decreases with a higher annealing temperature of the NiO layer. From the full XRD scans (displayed in **Supplementary Figure S2A**) the same crystallographic orientation is observed for all precursor samples.

To understand the change in crystallinity of the precursor, we conducted contact angle measurements of H_2O and di-iodomethane on the NiO surface. The contact angle of H_2O decreases from 65.8° on pristine NiO to 14.1° on NiO300 (see **Supplementary Figure S3**). Using the Owens, Wendt, Rabel and Kaelble method, the free surface energy was calculated, using the contact angles of H_2O as the polar solvent and of di-iodomethane as the non-polar solvent. The results are shown in **Figure 1F**. We measure an increase from 53 mN/m on pristine NiO to 79.5 mN/m on NiO300. The free surface energy is an essential driving force for the nucleation and subsequent growth behaviour during PVD (Thompson and Carel, 1995). Therefore, the different growth modes—leading to a flat, compact and well crystallized layers on pristine NiO and rough, disordered layers with a low crystallinity on NiO300—can be explained by the change of the free surface energy of the NiO upon annealing.

2.1.2 Annealing of the CsI/PbI_2 Precursor

Seeing that the CsI/PbI_2 precursor exhibits a different morphology and crystallinity depending on the surface properties of the NiO HTL, we have to consider if this also affect the properties of the final perovskite layers. However, during the initialization phase of our CVD process, the reactor is heated up and stabilized at the target temperature. This is essential to achieve stable reaction conditions (e.g., sublimation rate of organic precursor and reaction rate with the inorganic precursor). During this stage, a reverse flow of a carrier gas prevents the premature formation of perovskite phase, which means that the CsI/PbI_2 precursor undergoes an annealing treatment at 170°C/7 mbar before the actual conversion to perovskite phase is occurring. More details can be found in our previous work (Moser et al., 2020). Our investigations show that during this annealing phase of the CVD process, the precursor undergoes a strong structural transformation before the perovskite formation starts.

Using XRD, SEM and atomic force microscopy (AFM) a strong sintering of the CsI/PbI_2 precursor during said initialization phase of the CVD process is observed. In **Figures 2A–C** we display cross-sectional and top-view SEM images of the CsI/PbI_2 precursor grown on NiO300 in its as deposited state as

well as after 5 and 10 min of annealing in the CVD reactor. 10 min is the maximum annealing time as after this duration, the flow direction of the carrier gas would be reversed and the conversion process would begin. From the SEM cross-section images we can see how the disordered structure of the precursor turns into a compact layer. AFM measurements confirm that the precursor surface transforms from a rough landscape with protruding features to a flat planar surface. The root-mean-square (RMS) roughness of the three different surfaces is shown in **Figure 2D**. We see that through 10 min of annealing a near three-fold reduction of the roughness occurs.

XRD measurements show that the morphological transformation is also accompanied by a recrystallization. **Figure 2E** shows the FWHM and maximum intensity of the (001) peak of the PbI_2 phase before and after 5 or 10 min of annealing. The increasing peak intensity and simultaneously decreasing FWHM reveal a strong recrystallization due to the annealing. We note that the crystallographic orientation of the precursor is not changing during the recrystallization process. The full XRD scans are displayed in **Supplementary Figure S2B**.

For the as deposited precursor layer an average crystallite size of ~99 nm can be estimated with the Williamson-Hall method (Birkholz, 2005). This crystallite dimension corresponds well to the size of particles seen in the SEM cross-section micrograph of **Figure 2A**. After 5 and 10 min of annealing in the CVD the precursor an average crystallite size of 229 and 368 nm is calculated respectively. These values are not exact as the Williamson-Hall method loses its linearity for crystallite sizes over 100–200 nm. Still the result clearly shows that the crystallites fuse together upon annealing and larger grains are formed. The details regarding the calculations are given in the supplementary information and the corresponding Williamson-Hall plot is shown in **Supplementary Figure S4**.

These results show that the start-up phase of CVD process provides a homogenizing annealing treatment - in terms of structural properties - of the CsI/PbI_2 precursor. Thus, the surface properties of NiO are not expected to influence the structural properties of the perovskite layer. This can also be seen in **Supplementary Figure S5**, where the TE-CVD perovskite layers exhibit nearly identical morphology, irrespective of the HTL they were deposited on.

2.2 Perovskite Formation Process During CVD

In this section, we investigate the perovskite phase formation process by reaction of the metal halide precursor with FAI vapour. With our CVD system, we are able to conduct the conversion reaction for well-defined durations and obtain intermediate states of the precursor-to-perovskite transformation. A schematic of the CVD system is shown in **Supplementary Figure S6** and more details on the process are given in the materials and methods section.

We fabricated a series of samples, ranging from the pristine state of the precursor up to the full conversion (i.e., pure perovskite phase), which is reached after 20 min of the CVD process. After the CVD process, the films are not annealed or treated in any another way. The conversion was verified with XRD (see **Supplementary Figure S2C**) and UV-Vis (see **Supplementary Figure S7A**). The growth of the perovskite leads to a steady increase of the sub-bandgap asorption accompanied by an increase of the perovskite diffraction peak intensity. At the same time, the diffraction peaks of the precursor phase decreases and vanishes after 20 min of conversion. We point out that the perovskite phase maintains its crystallographic orientation during the whole conversion process.

2.2.1 Top Morphology

The top view SEM images and AFM scans of the series of samples are displayed in **Figures 3A–F**. After only 2.5 min of conversion reaction (see **Figure 3B**), the morphology of the surface has already changed considerably. A continuous perovskite layer has formed, which covers the underlying precursor layer (cross-section images are shown in **Figure 4**). From the SEM images no changes in grain size or shape of the perovskite are discernible over the course of the conversion process. Comparing metal halide precursor and perovskite, we see that the grain sizes and shapes are very similar. Thus, we hypothesize, that the individual grains of the precursor are converted to perovskite and that the original grain boundaries are maintained. Considering this, we see how important the microstructure of the metal halide precursor is for the CVD, as it will determine the perovskite morphology.

The RMS roughness calculated from AFM scans (see **Figure 3G**) support the observation from SEM. The surface roughness quickly evolves from a RMS roughness below 10 nm for the annealed precursor to over 20 nm after 2.5 min of conversion reaction. After this, the roughness only increases slightly for the whole rest of the conversion process. The increased roughness of the films is explained by the volumetric expansion during the phase transformation (Yang et al., 2015; Zhang et al., 2015).

To show that the final perovskite morphology is strongly dependent on the growth conditions and not on the precursor morphology alone, we also fabricated perovskite layers by spin-coating FAI on the metal halide precursor and reacting the two by annealing. These films exhibit much bigger grains of up to 2 μm (see **Supplementary Figure S8**). However, the conversion reaction is not well-controlled as can be seen by the much broader distribution of grain sizes. During CVD, continuous supply of low concentration of FAI vapour leads to a continuous, controlled conversion reaction. The grain-wise transformation of the inorganic precursor occurs with minor coalescence of smaller grains resulting in a perovskite layer with relatively small grains of 100–500 nm diameter.

2.2.2 Reaction Front and Diffusion

A barely discussed phenomena of two-step growth method of hybrid perovskites is the temporal and lateral evolution of the reaction front and the interdiffusion of inorganic and organic reactants. Here, we elucidate how the reaction front proceeds in a planar manner from top to bottom and how cesium is able to diffuse through the PbI_2 phase and is incorporated into the newly formed perovskite.

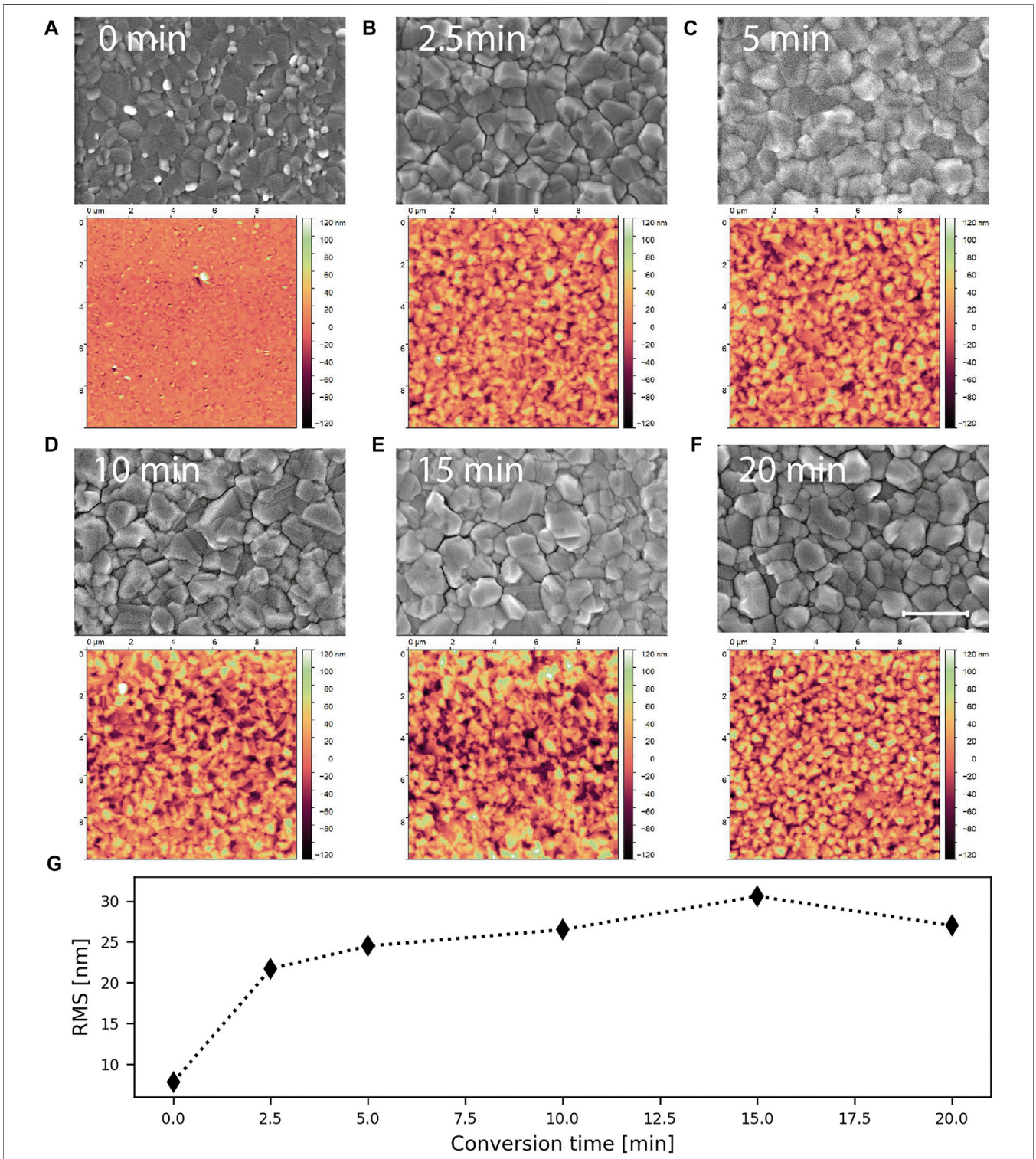

FIGURE 3 | Evolution of the top morphology during CVD. AFM scan and SEM top view image of the sample after **(A)** 0, **(B)** 2.5, **(C)** 5, **(D)** 10, **(E)** 15 and **(F)** 20 min of CVD. The scale bar corresponds to 1 µm and applies to all SEM images. **(G)** RMS roughness extracted from the AFM scans shown in **(A–F)**.

For this purpose, we conducted time-of-flight secondary ion mass spectrometry (ToF-SIMS) depth profiling of samples in the intermediate states of the TE-CVD deposition process. This includes also the as deposited CsI/PbI_2 precursor and the CsI/PbI_2 precursor after 10 min of annealing in the CVD, i.e. at the start of the CVD conversion process to which we refer as "0 min"

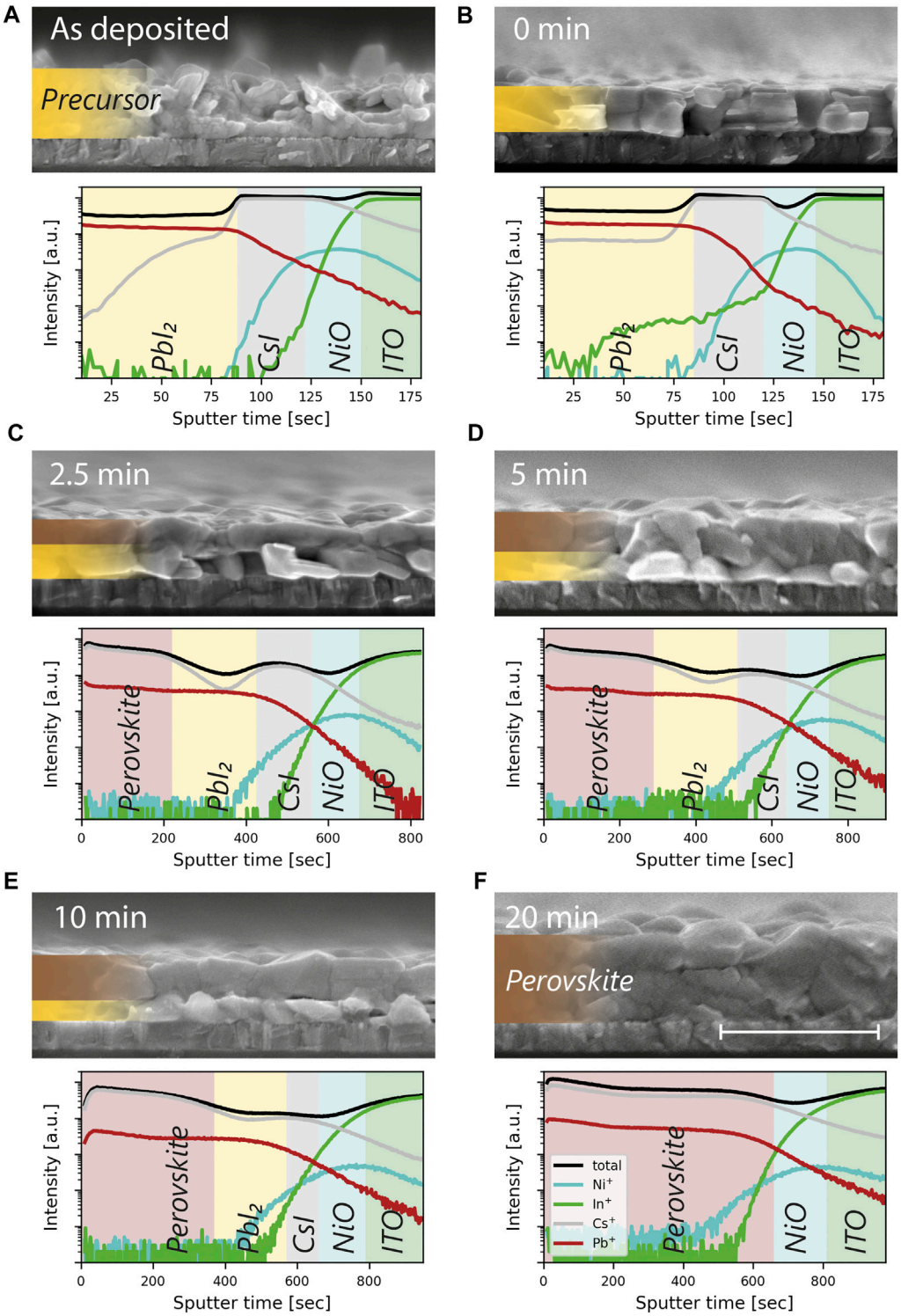

FIGURE 4 | Evolution of the reaction front and diffusion of cesium during CVD reaction. SIMS compositional profiles and SEM cross sections of the **(A)** as deposited metal halide precursor and intermediate states of the CVD process after **(B)** 0 min, **(C)** 2.5 min, **(D)** 5 min, **(E)** 10 min and **(F)** 20 min of reaction. The shadings in the SIMS profiles are meant as a guide to the eye and do not represent clear boundaries of the different layers. The scale bar for the SEM images corresponds to 1 µm and the legend in **(F)** applies to all SIMS profiles.

of conversion here. The depth profiles of the elements and the corresponding SEM cross section images are displayed in **Figures 4A–F**. Looking at the pristine CsI/PbI_2 precursor (see **Figure 4A**), the profiles show the stacking of PbI_2 on top of CsI of the layers by the decrease of Pb^+ and the step-like profile of Cs^+. This stacking remains intact even after the strong sintering due to the 10 min of annealing in the CVD (see **Figure 4B**). During this annealing process, cesium is diffusing into the PbI_2 layer as can be seen by the low but homogeneous distribution of Cs^+ in the PbI_2 layer. However, the individual CsI and PbI_2 layers are still present, as can be seen by the step-like profile of Cs^+. In the SIMS profile of **Figure 4B**, In^+ is apparently also present in the region of the CsI/PbI_2 precursor. We attribute this to a pinhole in the layer that allowed premature sputtering of the substrate and not an actual interdiffusion of indium into the precursor layer.

The following SIMS profiles and cross section SEM images of the intermediate states of the CVD conversion process reveal the movement of the conversion front from top to bottom and the opposing diffusion processes involved in the perovskite formation.

The SEM images of the intermediate states at 2.5, 5 and 10 min (i.e., **Figures 4C–E**) show a bilayer structure, where the unconverted inorganic precursor layer is sandwiched between the NiO coated substrate and the newly formed perovskite. From this planar movement of the reaction front towards the substrate, we can deduce the diffusion process of the FAI: During the CVD process, new FAI is supplied in vapour form to the sample surface. To continue the conversion reaction, the FAI needs to diffuse from the surface through the perovskite to reach the reaction front. This is only possible due to the high diffusivity of the FA^+ and I^- ions in the perovskite lattice. After 20 min of CVD full conversion is reached and no residual precursor phase is discernible in the SEM image.

The SIMS profiles on the other hand reveal how the diffusion of cesium contributes to the formation reaction. In the intermediate states after 2.5, 5 respectively 10 min, the cesium profile shows an intriguing feature: A dip in concentration between the top of the sample, where the perovskite has been formed and the position of the CsI layer. The Pb profile does not exhibit this behaviour and remains stable until the underlying CsI layer is reached. We attribute the dip to the lower concentration of cesium found in the PbI_2 phase (as was already observed for the sintered precursor in **Figure 4B**). This shows that during the CVD conversion reaction, the PbI_2 layer remains continuous but the Cesium is continuously diffusing through it to the reaction front. There it is participating in the formation reaction and incorporated into the freshly formed perovskite. Without this diffusion process—opposite to the one of FAI—the incorporation of Cs into the perovskite would only happen once the reaction front reaches the CsI layer and one would need to consider strong compositional gradients in the final absorber. Due to the efficient interdiffusion processes occuring, the final perovskite exhibits a homogeneous distribution of cesium as seen in **Figure 4F**.

2.2.3 Perovskite Composition

Using Tauc plots (displayed in **Supplementary Figures S7B–F**), an optical band gap of 1.55 eV is determined for all intermediate stages of the CVD process. This is also confirmed by steady-state photoluminescence (see **Supplementary Figure S9**), where we observe single peaks with maxima at 800 ± 2 nm (corresponding to a band gap of 1.549 eV). As the cesium content affects the band gap [1.527 and 1.565 eV for pure $FAPbI_3$ and for $Cs_{0.1}FA_{0.9}PbI_3$ respectively (Subedi et al., 2018)], this confirms that the cesium content is constant throughout the perovskite formation process. For a homogeneous distribution of cesium, we estimate a final perovskite composition of $Cs_{0.07}FA_{0.93}PbI_3$, using the thickness and bulk density of the CsI (15 nm, 4.51 g/cm^3) and PbI_2 (300 nm, 6.16 g/cm^3) layers. The composition was confirmed experimentally with X-ray photoelectron spectroscopy (see **Supplementary Figure S10**) of the perovskite after 20 min of CVD conversion, where an atomic Cs to Pb ratio of 7 to 100 was measured.

3 CONCLUSION

In this work, we have investigated the complete formation process of perovskite during two-step TE-CVD process. We demonstrate how the morphology and crystallinity of CsI/PbI_2 is affected by the surface properties of the underlying HTL layer. Due to a recrystallization process during the heat-up phase of the CVD reactor, the metal halide precursor morphology is homogenized before it is converted to perovskite. As a result, the conversion during the CVD process results in the same perovskite morphology, independent of the morphology of the pristine precursor.

Furthermore, we show how under the controlled conditions of the CVD process, the reaction front moves in a planar fashion from top to bottom. During this conversion reaction, two opposing diffusion processes are occurring. FAI is diffusing from the surface side, through the perovskite layer, while Cesium is diffusing from the substrate side through the PbI_2 layer to the reaction front. SIMS profiling reveals that by this diffusion process, cesium is incorporated into the perovskite from the very beginning and that the final perovskite possess a homogeneous elemental distribution. This shows that stacked metal halide layers are a viable precursor choice for perovskite formation by CVD.

4 MATERIALS AND METHODS

4.1 Materials

Patterned 2.5 cm × 2.5 cm ITO substrates (15 Ohm/sq) were bought from Advanced Election Technology Co. PEDOT:PSS solution was bought from Heraeus (Clevios P VP.Al 4083). CsI (>99%), PbI_2 (>99%) and FAI (>99.99%) were purchased from TCI chemicals. C_{60} and BCP were purchased from Xi'an Polymer Light Technology Corp.

4.2 Substrate Cleaning

Before the deposition, the ITO substrates were cleaned by 10 min of ultra-sonication in IPA, rinsed with deionized water, followed by soaking in a 1v% aqueous Hellmanex (Hellmanex III, Hellma

GmbH & Co.) solution for at least 10 h, rinsed again with deionized water and then ultra-sonicated for 20 min in deionized water. The cleaned substrates were stored in IPA and blown dry with a nitrogen gun before use.

4.3 HTL Deposition

Before deposition, the ITO substrates were subjected to 15 min of UV-Ozone cleaning (Jelight, Model 24).

NiO_x was deposited by RF magnetron sputtering from a NiO_x target (Disc AG, target diameter 100 mm) in an Evatec Clusterline cluster tool. The chuck temperature was set at 60°C. The sputtering power was set to 150 W and the deposition happened under an Ar gas flow of 150 sccm. The thickness is controlled by adjusting the deposition time. The base pressure in the deposition is about 7e-7 mbar and the working pressure is 6.7e-3 mbar.

The NiO layers were then either used directly (i.e. in its pristine form) or annealed at different temperatures (100, 200 or 300°C). For the annealing the substrates were placed on a hot plate at room temperature which was then heated to the target temperature at a rate of 20°C/min. Then the annealing was carried out for 15 min at the target temperature. After that, the hot plate was turned off and let cool down to below 100°C before taking the substrates off.

PEDOT:PSS layers were deposited by spin-coating. The purchased solution was used as is. For the spin-coating, 300 µL where dispensed through a 0.45 µm filter onto the substrate. Then the substrate was accelerated with 1,000 rpm/s for 1 s and then with 10,000 rpm/s up to 5,000 rpm and kept spinning for 45 s. The layers were dried on a hotplate at 150°C for 20 min.

4.4 Deposition of Inorganic Precursor

The stacked CsI/PbI_2 precursor was deposited by thermal evaporation controlled by a quartz crystal balance. The pressure of p < 1e-5 mbar was maintained during the evaporation. First, 15 nm CsI was evaporated at a rate of ~1.0 Å/s, followed by a 300 nm thick PbI_2 layer evaporated at ~2.0 Å/s. The nominal composition of $Cs_{0.07}FA_{0.93}PbI_3$ was calculated based on the thickness of the CsI and PbI_2 layer.

4.5 Chemical Vapour Deposition Conversion of Inorganic Precursor

The CVD set-up used for this work was described in detail in a previous publication (Moser et al., 2020). A schematic of the set-up is given in **Supplementary Figures S6A,B**. In short, the CVD conversion is carried out in a multi-zone tube furnace (Carbolite, HZS 12/900) at reduced pressure, using ambient air (relative humidity: 35–40%) as carrier gas. A graphite crucible (Umicore, ESQ 113) containing 0.2 g of FAI and the substrates coated with inorganic precursor are placed in separate heating zones. The tube furnace is equipped with a mass flow controller (Pfeiffer Vacuum, EVR 116) and valves that allow to create a precisely controlled flow of carrier gas in either direction through the tube. With this, the carrier gas can either flow from the graphite crucible towards ("forward flow") or away ("reverse flow") from the precursor substrates. Using the reverse flow of the carrier gas, the tube is pumped to the working pressure of 7 mbar and the heating zones are ramped to 170°C and 200°C for the precursor and the crucible zone respectively. The pressure is controlled by employing a constant gas flow of ambient air of 0.5 mbar*l/s and regulating the inlet of the vacuum pump (Edwards, RV 12) with a needle valve. Once the target temperatures are reached, the reverse flow is maintained for 10 min to allow for a stabilization of the temperature zones, while at the same time preventing the conversion reaction to occur prematurely. After that, the carrier gas flow is switched to forward flow. This starts the conversion reaction by the active transport of the FAI vapour to the precursor substrates. The conversion process is stopped after the desired time (2.5, 5, 10, 15, 20, 30, 40 min in this work) by switching back to the reverse flow of the carrier gas. The reverse flow is kept for 4 min to remove all FAI residues from the substrates before venting the tube and taking out the substrates. A generalized visual representation of the process is given in **Supplementary Figure S6C**.

4.6 Material Characterizations

X-Ray diffraction patterns were measured with an X'Pert Pro in Bragg-Brentano geometry using Cu-Kα1 radiation (λ = 1.5406 Å), scanning from 5 to 60° (2θ) with a step interval of 0.0167°. Full-width at half-maximum and maximal intensity of the peaks were obtained by fitting a Gaussian peak with Origin 2020b.

Transmittance measurements in the range from 300 to 1,500 nm were performed using a Shimadzu UV-Vis 3600 spectrophotometer equipped with an integrating sphere.

A Hitachi S-4800 Scanning Electron Microscope was used for the imaging of top view and cross-sections. A 5 kV acceleration voltage was used for a 10 mA probing beam. A Pt coating (~1 .5 nm) was used to decrease charging effects.

AFM images of an area of 10 µm × 10 µm were taken in ambient air on a Bruker ICON3 in tapping mode. A silicon nitride tip with 10 nm radius (ScanAsyst-air), 0.4 N/m cantilever spring constant and 70 kHz resonant frequency was used as probe. The open-source software Gwyddion was used for post-process flattening of the scans and the calculation of the surface roughness.

Compositional depth profiles were measured by ToF-SIMS (ION-TOF, TOF-SIMS 5). The primary beam was a 25 keV Bi^+ with total current of 0.39 pA and a raster size of 50 × 50 μm^2. The sputtering beam was a 50 nA, 2 keV O_2^+ with an on-sample area of 300 × 300 μm^2

Contact angle measurements were carried out on a drop shape analyzer (Krüss, DSA30E). Contact angles of droplets of deionized water and di-iodomethane were measured by a Young-Laplace fit of the drop shape. The free surface energy was calculated with the OWRK model.

X-ray photoelectron spectroscopy was performed using a Quantum2000 system from Physical Electronics with a monochromatic Al Ka source (1,486.6 eV) and a base pressure below 8 × 10–9 mbar. A 2 min ion sputtering step was performed using a beam energy of 0.5 keV before measurement to measure at an approximate depth of 50 nm. The high-resolution scan of

the Pb 4f and Cs 3d spectra was acquired with a step size of 0.25 eV and a pass energy of 29.30 eV. A charge neutralizer was used for charge compensation. The atomic percentage (at%) was evaluated using Multipak software.

DATA AVAILABILITY STATEMENT

The raw data supporting the conclusion of this article will be made available by the authors, without undue reservation.

AUTHOR CONTRIBUTIONS

TM planned and executed the experiments and prepared the manuscript. RK conducted AFM measurements, SY conducted SIMS profiling. HL contributed to the HTL development and SIMS measurements. AW deposited NiO by RF sputtering, SS conducted contact angle measurements, EG conducted XPS measurement and analysis, AT and FF supervised the work. All authors participated in the discussion and manuscript revision.

FUNDING

We gratefully acknowledge funding from the Swiss Federal Office for Energy (SFOE) for the project "CIGSPSC" (Grant number: SI/501805-01). Open access funding provided by Empa—Swiss Federal Laboratories for Materials Science and Technology.

SUPPLEMENTARY MATERIAL

The Supplementary Material for this article can be found online at: https://www.frontiersin.org/articles/10.3389/fenrg.2022.883882/full#supplementary-material

REFERENCES

Abzieher, T., Moghadamzadeh, S., Schackmar, F., Eggers, H., Sutterlüti, F., Farooq, A., et al. (2020). Progress on Perovskite Solar Cells with All-Inkjet-Printed Absorber and Extraction Layers. *Adv. Energy Mater.* 0, 1802995. doi:10.1364/PVLED.2020.PvW2G.5

Ávila, J., Momblona, C., Boix, P. P., Sessolo, M., and Bolink, H. J. (2017). Vapor-Deposited Perovskites: The Route to High-Performance Solar Cell Production? *Joule* 1, 431–442. doi:10.1016/j.joule.2017.07.014

Aydin, E., Troughton, J., De Bastiani, M., Ugur, E., Sajjad, M., Alzahrani, A., et al. (2018). Room-Temperature-Sputtered Nanocrystalline Nickel Oxide as Hole Transport Layer for P-I-N Perovskite Solar Cells. *ACS Appl. Energy Mat.* 1, 6227–6233. doi:10.1021/acsaem.8b01263

Birkholz, M. (2005). *Thin Film Analysis by X-Ray Scattering*. Weinheim, Germany: John Wiley & Sons, 85–141.

Bishop, J. E., Read, C. D., Smith, J. A., Routledge, T. J., and Lidzey, D. G. (2020). Fully Spray-Coated Triple-Cation Perovskite Solar Cells. *Sci. Rep.* 10, 6610. doi:10.1038/s41598-020-63674-5

Bishop, J. E., Smith, J. A., and Lidzey, D. G. (2020). Development of Spray-Coated Perovskite Solar Cells. *ACS Appl. Mat. Interfaces* 12, 48237–48245. doi:10.1021/acsami.0c14540

Boyd, C. C., Shallcross, R. C., Moot, T., Kerner, R., Bertoluzzi, L., Onno, A., et al. (2020). Overcoming Redox Reactions at Perovskite-Nickel Oxide Interfaces to Boost Voltages in Perovskite Solar Cells. *Joule* 4, 1759–1775. doi:10.1016/j.joule.2020.06.004

Chen, Q., Zhou, H., Hong, Z., Luo, S., Duan, H.-S., Wang, H.-H., et al. (2014). Planar Heterojunction Perovskite Solar Cells via Vapor-Assisted Solution Process. *J. Am. Chem. Soc.* 136, 622–625. doi:10.1021/ja411509g

Chiang, Y.-H., Anaya, M., and Stranks, S. D. (2020). Multisource Vacuum Deposition of Methylammonium-free Perovskite Solar Cells. *ACS Energy Lett.* 5, 2498–2504. doi:10.1021/acsenergylett.0c00839

Du, M., Zhu, X., Wang, L., Wang, H., Feng, J., Jiang, X., et al. (2020). High-Pressure Nitrogen-Extraction and Effective Passivation to Attain Highest Large-Area Perovskite Solar Module Efficiency. *Adv. Mater.* 32, 2004979. doi:10.1002/adma.202004979

Eggers, H., Schackmar, F., Abzieher, T., Sun, Q., Lemmer, U., Vaynzof, Y., et al. (2020). Inkjet-Printed Micrometer-Thick Perovskite Solar Cells with Large Columnar Grains. *Adv. Energy Mat.* 10, 1903184. doi:10.1002/aenm.201903184

Feng, J., Jiao, Y., Wang, H., Zhu, X., Sun, Y., Du, M., et al. (2021). High-throughput Large-Area Vacuum Deposition for High-Performance Formamidine-Based Perovskite Solar Cells. *Energy Environ. Sci.* 14, 3035–3043. doi:10.1039/D1EE00634G

Guesnay, Q., Sahli, F., Ballif, C., and Jeangros, Q. (2021). Vapor Deposition of Metal Halide Perovskite Thin Films: Process Control Strategies to Shape Layer Properties. *Apl. Mater.* 9, 100703. doi:10.1063/5.0060642

Guo, P., Zhu, H., Zhao, W., Liu, C., Zhu, L., Ye, Q., et al. (2021). Interfacial Embedding of Laser-Manufactured Fluorinated Gold Clusters Enabling Stable Perovskite Solar Cells with Efficiency over 24%. *Adv. Mater.* 33, 2101590. doi:10.1002/adma.202101590

Heo, J. H., Lee, M. H., Jang, M. H., and Im, S. H. (2016). Highly Efficient CH3NH3PbI3−xClx Mixed Halide Perovskite Solar Cells Prepared by Re-dissolution and Crystal Grain Growth via Spray Coating. *J. Mat. Chem. A* 4, 17636–17642. doi:10.1039/c6ta06718b

Hoerantner, M. T., Wassweiler, E. L., Zhang, H., Panda, A., Nasilowski, M., Osherov, A., et al. (2019). High-Speed Vapor Transport Deposition of Perovskite Thin Films. *ACS Appl. Mat. Interfaces* 11, 32928–32936. doi:10.1021/acsami.9b07651

Jeong, J., Kim, M., Seo, J., Lu, H., Ahlawat, P., Mishra, A., et al. (2021). Pseudo-halide Anion Engineering for α-FAPbI3 Perovskite Solar Cells. *Nature* 592, 381–385. doi:10.1038/s41586-021-03406-5

Jošt, M., Kegelmann, L., Korte, L., and Albrecht, S. (2020). Monolithic Perovskite Tandem Solar Cells: A Review of the Present Status and Advanced Characterization Methods toward 30% Efficiency. *Adv. Energy Mater.* 10, 1904102. doi:10.1002/aenm.201904102

Kothandaraman, R. K., Jiang, Y., Feurer, T., Tiwari, A. N., and Fu, F. (2020). Near-Infrared-Transparent Perovskite Solar Cells and Perovskite-Based Tandem Photovoltaics. *Small Methods* 4, 2000395. doi:10.1002/smtd.202000395

Leyden, M. R., Ono, L. K., Raga, S. R., Kato, Y., Wang, S., and Qi, Y. (2014). High Performance Perovskite Solar Cells by Hybrid Chemical Vapor Deposition. *J. Mat. Chem. A* 2, 18742–18745. doi:10.1039/c4ta04385e

Li, J., Wang, H., Chin, X. Y., Dewi, H. A., Vergeer, K., Goh, T. W., et al. (2020). Highly Efficient Thermally Co-evaporated Perovskite Solar Cells and Mini-Modules. *Joule* 4, 1035–1053. doi:10.1016/j.joule.2020.03.005

Liu, G., Zheng, H., Ye, J., Xu, S., Zhang, L., Xu, H., et al. (2021). Mixed-Phase Low-Dimensional Perovskite-Assisted Interfacial Lead Directional Management for Stable Perovskite Solar Cells with Efficiency over 24%. *ACS Energy Lett.* 6, 4395–4404. doi:10.1021/acsenergylett.1c01878

Liu, J., Shi, B., Xu, Q., Li, Y., Chen, B., Wang, Q., et al. (2021). Crystalline Quality Control in Sequential Vapor Deposited Perovskite Film toward High Efficiency and Large Scale Solar Cells. *Sol. Energy Mater. Sol. Cells* 233, 111382. doi:10.1016/j.solmat.2021.111382

Luo, L., Ku, Z., Li, W., Zheng, X., Li, X., Huang, F., et al. (2021). 19.59% Efficiency from Rb0.04-Cs0.14FA0.86Pb(Br I1−)3 Perovskite Solar Cells Made by Vapor-Solid Reaction Technique. *Sci. Bull.* 66, 962–964. doi:10.1016/j.scib.2021.01.031

Luo, P., Liu, Z., Xia, W., Yuan, C., Cheng, J., and Lu, Y. (2015). A Simple *In Situ* Tubular Chemical Vapor Deposition Processing of Large-Scale Efficient Perovskite Solar Cells and the Research on Their Novel Roll-Over Phenomenon in J-V Curves. *J. Mat. Chem. A* 3, 12443–12451. doi:10.1039/c5ta02306h

Ma, F., Zhao, Y., Li, J., Zhang, X., Gu, H., and You, J. (2021). Nickel Oxide for Inverted Structure Perovskite Solar Cells. *J. Energy Chem.* 52, 393–411. doi:10.1016/j.jechem.2020.04.027

Mann, D. S., Patil, P., Kwon, S.-N., and Na, S.-I. (2021). Enhanced Performance of P-I-N Perovskite Solar Cell via Defect Passivation of Nickel Oxide/perovskite Interface with Self-Assembled Monolayer. *Appl. Surf. Sci.* 560, 149973. doi:10.1016/j.apsusc.2021.149973

Moser, T., Artuk, K., Jiang, Y., Feurer, T., Gilshtein, E., Tiwari, A. N., et al. (2020). Revealing the Perovskite Formation Kinetics during Chemical Vapour Deposition. *J. Mat. Chem. A* 8, 21973–21982. doi:10.1039/D0TA04501B

National Renewable Energy Laboratory (2020). NREL Best Research-Cell Efficiency Chart. AvaliableAt: https://www.nrel.gov/pv/assets/pdfs/best-research-cell-efficiencies.20200406.pdf (accessed April 14, 2020).

Newman, R., and Chrenko, R. M. (1959). Optical Properties of Nickel Oxide. *Phys. Rev.* 114, 1507–1513. doi:10.1103/physrev.114.1507

Niu, G., Wang, S., Li, J., Li, W., and Wang, L. (2018). Oxygen Doping in Nickel Oxide for Highly Efficient Planar Perovskite Solar Cells. *J. Mat. Chem. A* 6, 4721–4728. doi:10.1039/c8ta00161h

Pang, S., Zhang, C., Dong, H., Chen, D., Zhu, W., Xi, H., et al. (2019). Efficient NiOx Hole Transporting Layer Obtained by the Oxidation of Metal Nickel Film for Perovskite Solar Cells. *ACS Appl. Energy Mat.* 2, 4700–4707. doi:10.1021/acsaem.9b00169

Park, N.-G., and Zhu, K. (2020). Scalable Fabrication and Coating Methods for Perovskite Solar Cells and Solar Modules. *Nat. Rev. Mater* 5, 333–350. doi:10.1038/s41578-019-0176-2

Patidar, R., Burkitt, D., Hooper, K., Richards, D., and Watson, T. (2020). Slot-die Coating of Perovskite Solar Cells: An Overview. *Mater. Today Commun.* 22, 100808. doi:10.1016/j.mtcomm.2019.100808

Razza, S., Di Giacomo, F., Matteocci, F., Cinà, L., Palma, A. L., Casaluci, S., et al. (2015). Perovskite Solar Cells and Large Area Modules (100 Cm 2) Based on an Air Flow-Assisted PbI 2 Blade Coating Deposition Process. *J. Power Sources* 277, 286–291. doi:10.1016/j.jpowsour.2014.12.008

Powell, R. C., Research Leading to High Throughput Manufacturing of Thin-Film CdTe PV Modules: Annual Subcontract Report, 2006.

Sahli, F., Miaz, N., Salsi, N., Bucher, C., Schafflützel, A., Guesnay, Q., et al. (2021). Vapor Transport Deposition of Methylammonium Iodide for Perovskite Solar Cells. *ACS Appl. Energy Mat.* 4, 4333–4343. doi:10.1021/acsaem.0c02999

Saranin, D., Komaricheva, T., Luchnikov, L., Muratov, D. S., Le, T. S., Karpov, Y., et al. (2021). Hysteresis-free Perovskite Solar Cells with Compact and Nanoparticle NiO for Indoor Application. *Sol. Energy Mater. Sol. Cells* 227, 111095. doi:10.1016/j.solmat.2021.111095

Schackmar, F., Eggers, H., Frericks, M., Richards, B. S., Lemmer, U., Hernandez-Sosa, G., et al. (2021). Perovskite Solar Cells with All-Inkjet-Printed Absorber and Charge Transport Layers. *Adv. Mat. Technol.* 6, 2000271. doi:10.1002/admt.202000271

Shen, P.-S., Chen, J.-S., Chiang, Y.-H., Li, M.-H., Guo, T.-F., and Chen, P. (2016). Low-Pressure Hybrid Chemical Vapor Growth for Efficient Perovskite Solar Cells and Large-Area Module. *Adv. Mat. Interfaces* 3, 1500849. doi:10.1002/admi.201500849

Siegrist, S., Yang, S.-C., Gilshtein, E., Sun, X., Tiwari, A. N., and Fu, F. (2021). Triple-cation Perovskite Solar Cells Fabricated by a Hybrid PVD/blade Coating Process Using Green Solvents. *J. Mat. Chem. A* 9, 26680–26687. doi:10.1039/d1ta07579a

Subedi, B., Guan, L., Yu, Y., Ghimire, K., Uprety, P., Yan, Y., et al. (2018). Formamidinium + Cesium Lead Triiodide Perovskites: Discrepancies between Thin Film Optical Absorption and Solar Cell Efficiency. *Sol. Energy Mater. Sol. Cells* 188, 228–233. doi:10.1016/j.solmat.2018.09.002

Swartwout, R., Hoerantner, M. T., and Bulović, V. (2019). Scalable Deposition Methods for Large-area Production of Perovskite Thin Films. *Energy Environ. Mat.* 2, 119–145. doi:10.1002/eem2.12043

Thompson, C. V., and Carel, R. (1995). Texture Development in Polycrystalline Thin Films. *Mater. Sci. Eng. B* 32, 211–219. doi:10.1016/0921-5107(95)03011-5

Wei, X., Peng, Y., Jing, G., Simon, T., and Cui, T. (2021). High-Performance Perovskite Solar Cells Fabricated by a Hybrid Physical-Chemical Vapor Deposition. *J. Sol. Energy Eng.* 143, 041006. doi:10.1115/1.4049326

Yang, W. S., Noh, J. H., Jeon, N. J., Kim, Y. C., Ryu, S., Seo, J., et al. (2015). High-performance Photovoltaic Perovskite Layers Fabricated through Intramolecular Exchange. *Science* 348, 1234–1237. doi:10.1126/science.aaa9272

Yoo, J. J., Seo, G., Chua, M. R., Park, T. G., Lu, Y., Rotermund, F., et al. (2021). Efficient Perovskite Solar Cells via Improved Carrier Management. *Nature* 590, 587–593. doi:10.1038/s41586-021-03285-w

Yoshikawa, K., Kawasaki, H., Yoshida, W., Irie, T., Konishi, K., Nakano, K., et al. (2017). Silicon Heterojunction Solar Cell with Interdigitated Back Contacts for a Photoconversion Efficiency over 26%. *Nat. Energy* 2, 1–8. doi:10.1038/nenergy.2017.32

Zhang, H., Eickemeyer, F. T., Zhou, Z., Mladenović, M., Jahanbakhshi, F., Merten, L., et al. (2021). Multimodal Host–Guest Complexation for Efficient and Stable Perovskite Photovoltaics. *Nat. Commun.* 12, 3383. doi:10.5281/zenodo.4768098

Zhang, J., Long, J., Huang, Z., Yang, J., Li, X., Dai, R., et al. (2021). Obstructing Interfacial Reaction between NiOx and Perovskite to Enable Efficient and Stable Inverted Perovskite Solar Cells. *Chem. Eng. J.* 426, 131357. doi:10.1016/j.cej.2021.131357

Zhang, T., Yang, M., Zhao, Y., and Zhu, K. (2015). Controllable Sequential Deposition of Planar CH3NH3PbI3 Perovskite Films via Adjustable Volume Expansion. *Nano Lett.* 15, 3959–3963. doi:10.1021/acs.nanolett.5b00843

Zhao, X., Chen, J., and Park, N. G. (2019). Importance of Oxygen Partial Pressure in Annealing NiO Film for High Efficiency Inverted Perovskite Solar Cells. *Sol. RRL* 3, 1800339. doi:10.1002/solr.201800339

Conflict of Interest: The authors declare that the research was conducted in the absence of any commercial or financial relationships that could be construed as a potential conflict of interest.

Publisher's Note: All claims expressed in this article are solely those of the authors and do not necessarily represent those of their affiliated organizations, or those of the publisher, the editors and the reviewers. Any product that may be evaluated in this article, or claim that may be made by its manufacturer, is not guaranteed or endorsed by the publisher.